

Nested Configuration of Silicon Microring Resonator With Multiple Coupling Regimes

Jiayang Wu, Pan Cao, Xiaofeng Hu, Tao Wang, Mu Xu, Xinhong Jiang, Fei Li, Linjie Zhou, *Member, IEEE*, and Yikai Su, *Senior Member, IEEE*

Abstract—We propose and demonstrate a nested configuration of a silicon microring resonator possessing multiple coupling regimes in one passive device. For different resonance notches of the transmission intensity spectrum, diverse notch depths and bandwidths owing to multiple coupling regimes are designed and experimentally achieved. The phase response of the proposed configuration is also investigated. Experimental observation of fast and slow lights at different resonance wavelengths further verifies the realization of multiple coupling regimes.

Index Terms—Multiple coupling regimes, nested configuration, passive device, silicon microring resonator (MRRs).

I. INTRODUCTION

SILICON microring resonators (MRRs) have found wide applications in the past two decades along with the advance of micro/nanofabrication technologies [1]. Based on the simple ring resonators, various functional devices such as filters, modulators, switches, buffers, and sensors were proposed and some were experimentally demonstrated [2]–[6]. The compactness, CMOS compatibility, and agile applications of MRRs have made them key building blocks for future photonic integrated circuits.

For a typical single MRR consisting of a microring side-coupled to a straight waveguide, there exist three possible coupling regimes depending on the balance between the external coupling strength and the intrinsic cavity loss, namely over coupling, critical coupling, and under coupling. Each coupling regime has its own intensity and phase responses [1]. Based on these multiple coupling regimes, diverse applications in optical signal processing have been demonstrated, such as fast/slow light [7], [8], intensity/phase modulation [9], [10], and reconfigurable filtering [11]. However, for passive devices, both the external coupling strength and the intrinsic cavity loss are almost fixed once they are fabricated, which means

Manuscript received October 7, 2012; revised January 20, 2013; accepted January 28, 2013. Date of publication February 1, 2013; date of current version February 27, 2013. This work was supported in part by the National Science Foundation of China under Grant 61077052/61125504/61235007, in part by MoE under Grant 20110073110012, and in part by the Science and Technology Commission of Shanghai Municipality under Grant 11530700400.

The authors are with the Department of Electronic Engineering, State Key Laboratory of Advanced Optical Communication Systems and Networks, Shanghai Jiao Tong University, Shanghai 200240, China (e-mail: jiayangwu@sjtu.edu.cn; caopan@sjtu.edu.cn; huxf@sjtu.edu.cn; wangtao2007@sjtu.edu.cn; xumu@sjtu.edu.cn; jiangxinhong@sjtu.edu.cn; feili2010@sjtu.edu.cn; ljzhou@sjtu.edu.cn; yikaisu@sjtu.edu.cn).

Color versions of one or more of the figures in this letter are available online at <http://ieeexplore.ieee.org>.

Digital Object Identifier 10.1109/LPT.2013.2244589

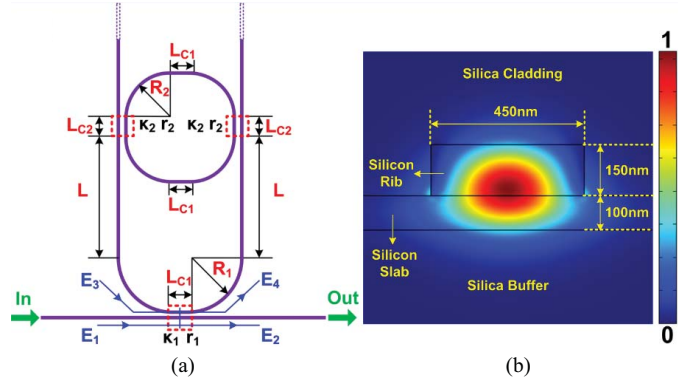


Fig. 1. (a) Schematic diagram of the proposed nested configuration of silicon MRR. (b) Cross section of the waveguide, with an overlay of the optical mode intensity plot given by FDTD simulations.

it is difficult to realize all these three coupling regimes in a single MRR. Moreover, it is also hard to control the fabrication to achieve a specific coupling regime, especially the quasi-critical coupling. To deal with this problem, some schemes in light of active tuning have been proposed [12]–[14]. However, the stringent requirements for the design and fabrication of active tuning modules would bring additional complexity and increase the fabrication cost.

In this letter, we propose and demonstrate a passive device based on nested configuration of silicon MRR to achieve multiple coupling regimes. For resonances at different wavelengths, multiple coupling regimes of over coupling, under coupling and quasi-critical coupling are obtained, which is demonstrated by measured transmission intensity spectrum with diverse resonance notch depths and bandwidths as well as experimental observation of fast and slow lights at different resonance wavelengths. Compared with devices based on active tuning, the design and the fabrication are much simpler, thus reducing the fabrication cost. On the other hand, compared with conventional MRRs, the proposed device provides richer spectrum with diverse intensity and phase responses.

II. DEVICE STRUCTURE AND OPERATION PRINCIPLE

Fig. 1(a) illustrates the schematic of the configuration that we propose: a microring is nested inside a U-bend waveguide, which forms a larger resonant loop. Another bus waveguide is side-coupled to the bottom of the U-bend waveguide to act as system input/output. From the transfer function of the drop port in an add-drop MRR [10], we obtain the relation between

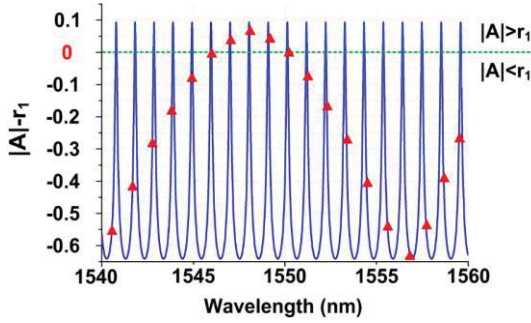


Fig. 2. Operation principle of realizing multiple coupling regimes.

E_3 and E_4 depicted in Fig. 1(a) as follows:

$$\frac{E_3}{E_4} = \frac{-\kappa_2^2 a_1^2 a_2 e^{i(2\phi_1+\phi_2)}}{1 - r_2^2 a_2^2 e^{i(2\phi_2)}} = |A| e^{i\Phi}, \quad (1)$$

where r_i and κ_i ($i = 1, 2$) are the transmission and coupling coefficients of the two kinds of couplers depicted in Fig. 1(a), respectively. $\phi_{1,2} = kL_{1,2}$, with k denoting the propagation constant, are the phase changes associated with the waveguides with lengths of half-length of the U-bend waveguide $L_1 = (\pi R_1 + L_{c1} + L_{c2})/2 + L$ and half-circumference of the nested microring $L_2 = \pi R_2 + L_{c1} + L_{c2}$, respectively. $a_{1,2} = \exp(-\alpha L_{1,2}/2)$, with α denoting the loss factor, are the transmission factors associated with the waveguides with lengths of $L_{1,2}$, respectively. $|A|$ and Φ are the amplitude and phase of the complex ratio, respectively. Then the transfer function of the proposed configuration obtained by using the scattering matrix method [15] can be written as follows:

$$\frac{E_2}{E_1} = \frac{r_1 - |A| e^{i\Phi}}{1 - r_1 |A| e^{i\Phi}} = \frac{r_1 - r_1 r_2^2 a_2^2 e^{i(2\phi_2)} + \kappa_2^2 a_1^2 a_2 e^{i(2\phi_1+\phi_2)}}{1 - r_2^2 a_2^2 e^{i(2\phi_2)} + r_1 \kappa_2^2 a_1^2 a_2 e^{i(2\phi_1+\phi_2)}}. \quad (2)$$

The cross-section of the waveguide is shown in Fig. 1(b), a 100-nm-thick silicon slab is used to reduce the scattering loss at sidewalls. Other structural parameters are chosen as follows: The gap size is $0.18 \mu\text{m}$ due to fabrication limitation; the coupling lengths are chosen to be $L_{c1} = L_{c2} = 7 \mu\text{m}$, thus strong coupling with $r_i \approx 0.84$ ($i = 1, 2$) could be achieved based on our previously fabricated devices; the ring radius is $R_2 = 80 \mu\text{m}$ to obtain a small free spectral range (FSR) so that there could be more resonances in the C band; and $L = 248 \mu\text{m}$ to avoid phase-matching where $2L_1 \approx nL_2$ (n is an integer). We use Lumerial finite-difference 2-D (FDTD) solutions for 2-D simulations, and the obtained transmission coefficients of the couplers are $r_1 = r_2 = 0.8250$. We also assume that the waveguide group index of the transverse electric (TE) mode is $n_g = 4.3350$ and the waveguide loss factor is $\alpha = 80 \text{ m}^{-1}$ (1.8 dB/cm) based on our previously fabricated devices. Thus the device works under strong coupling and low loss condition.

In Fig. 2, we plot $|A|-r_1$ obtained from (1) for various wavelengths in the range of $1540 \sim 1560 \text{ nm}$. The resonance wavelengths that satisfy $\hat{\phi} = 2m\pi$ (m is an integer) are also shown by red triangles on the curve. If we treat the proposed nested configuration as an equivalent single MRR, then $|A|$, r_1 , and $\hat{\phi}$ can be regarded as the equivalent round-trip transmission factor, transmission coefficient, and round-trip

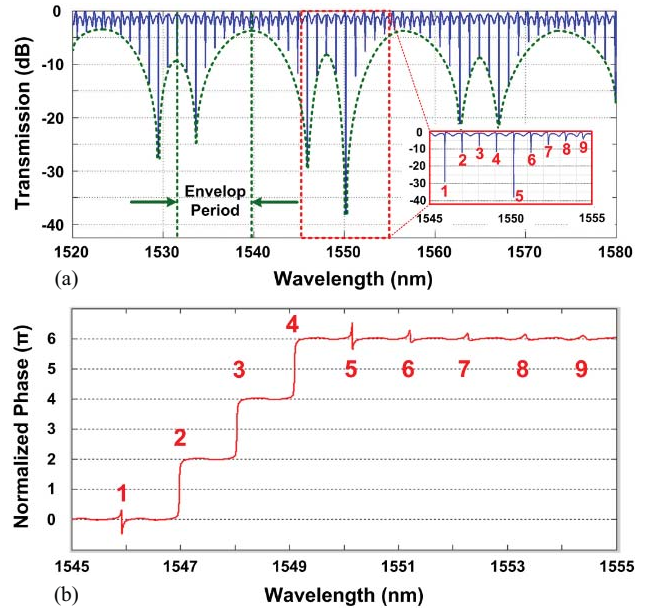


Fig. 3. (a) Normalized transmission intensity response of the proposed configuration. Zoom-in view around the deepest notch is shown in the inset. (b) Normalized transmission phase response around the deepest notch.

TABLE I
DEPTHS AND BANDWIDTHS FOR NOTCHES 1 ~ 9 IN THE INSET
OF FIG. 3(a)

Notch Number	1	2	3	4	5	6	7	8	9
Notch depth (dB)	29.0	12.1	7.9	11.8	38.0	12.2	7.7	5.4	4.1
Notch 3-dB bandwidth (pm)	53	45	40	46	54	65	77	86	96

phase, respectively. When $|A| > r_1$, $|A| = r_1$, and $|A| < r_1$ are satisfied, coupling regimes of over coupling, critical coupling, and under coupling can be achieved, respectively. From Fig. 2 we notice that some triangles lie in the region of $|A| > r_1$, some are in the region of $|A| < r_1$, and in particular, several triangles almost lie on the dividing line. That means the corresponding multiple coupling regimes are achieved at different resonance wavelengths, i.e., multiple coupling regimes are realized in the proposed passive device, rather than a specific coupling regime as in a single MRR. This is also verified by the normalized transmission intensity and phase responses obtained from (2), as illustrated in Fig. 3(a) and (b), respectively. The resonance intensity and phase responses corresponding to the three coupling regimes are observed despite of slight ripples between adjacent notches. Resonance notches with various depths and 3-dB bandwidths are uniformly spaced in the transmission intensity spectrum. The depths and 3-dB bandwidths of various resonance notches labeled as 1 ~ 9 in the inset of Fig. 3(a) are shown in Table I. The proposed device possesses a periodically varying resonance-notch envelop, and the envelop period covering several FSRs is shown in Fig. 3(a). Under the phase-mismatched condition, a shorter L leads to a smaller envelop period, but there would be fewer resonances in the over coupling regime. Therefore a trade-off is made when choosing the length of L . Under the condition of lower

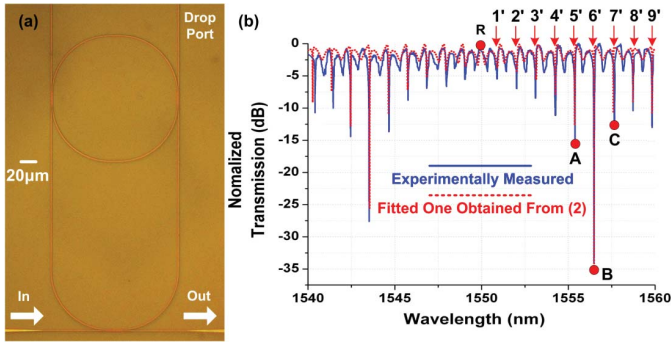


Fig. 4. (a) Micrograph of the fabricated device. (b) Experimentally measured spectral response of normalized transmission intensity (blue solid curve) and the fitted one obtained from (2) (red dashed curve).

loss or stronger coupling, the maximum value of $|A| - r_1$ becomes larger, thus leading to more red triangles above the dividing line in Fig. 2 and providing more resonances in the over coupling regime.

III. DEVICE FABRICATION AND MEASURED SPECTRUM

The proposed device based on the above design parameters is fabricated on an 8-inch silicon-on-insulator (SOI) wafer with a 250-nm-thick top silicon layer and a 3- μ m-thick buried dioxide layer. The micrograph of the fabricated device is shown in Fig. 4(a). 248-nm deep ultraviolet (DUV) photolithography is utilized to define the pattern and an inductively coupled plasma (ICP) etching process is used to etch the top silicon layer. Lower scattering loss and smaller gap size could be achieved by more accurate e-beam lithography. A 1.5- μ m-thick silica layer is deposited by plasma enhanced chemical vapor deposition (PECVD) to cover the whole device as upper cladding [16]. Grating couplers for TE polarization are employed at each end of the four ports in Fig. 4(a) to couple light into/out of the device with single-mode fibers as well as to taper away undesired signal at the drop port.

The blue solid curve in Fig. 4(b) presents the experimentally measured normalized transmission intensity spectrum of the proposed device. The on-chip insertion loss is ~ 10.5 dB. The measured depths and 3-dB bandwidths of various resonance notches labeled as $1' \sim 9'$ in Fig. 4(b) are shown in Table II, where a resonance notch with a depth of ~ 35.2 dB is noticeable. The measured curve is fitted by the red dashed curve obtained from (2). The fitting parameters are $r_1 = r_2 \approx 0.8232$, $\alpha \approx 72 \text{ m}^{-1}$ (1.6 dB/cm), and $n_g \approx 4.17395$. The discrepancies between the fitting parameters and the design parameters lead to a shift of the resonance notch envelope in the transmission intensity spectrum but do not significantly affect the shape of the envelope. Practically, the proposed device is more robust against fabrication errors, since one can always find a suitable coupling regime within an envelope period. It can be seen from Fig. 4(b) that the measured curve fits well with the one obtained from (2), except for slight attenuation at shorter wavelengths that could be attributed to the limited transmission bandwidth of the grating couplers. Another factor leading to the discrepancy between the two curves is the slight variation of the coupling coefficients due to wavelength change [17].

TABLE II
DEPTHS, BANDWIDTHS, AND PULSE DELAYS FOR
NOTCHES $1' \sim 9'$ IN FIG. 4(b)

Notch Number	$1'$	$2'$	$3'$	$4'$	$5'$	$6'$	$7'$	$8'$	$9'$
Notch depth (dB)	5.8	7.1	8.5	11.5	15.0	35.2	12.7	10.5	12.8
Notch 3-dB bandwidth (pm)	99	92	86	78	68	60	54	49	53
Pulse delay (ps)	≈ 0	-3	-6	-15	-32	▲	84	48	78

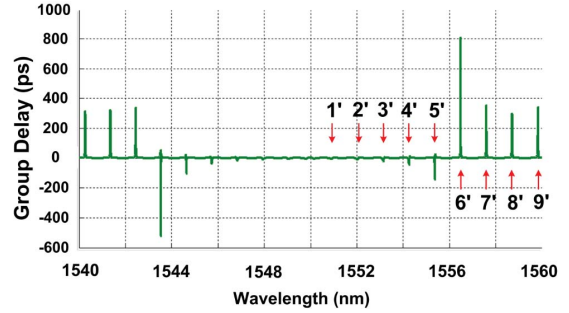


Fig. 5. Calculated GD response of the proposed device using the fitting parameters obtained from the measured transmission intensity spectrum. Dips $1' \sim 5'$ and peaks $6' \sim 9'$ correspond to resonance notches $1' \sim 9'$ in Fig. 4(b).

IV. EXPERIMENT OF FAST/SLOW LIGHT

In addition to the intensity response, the phase response of the proposed device is also investigated. The group delay (GD) is given by the angular-frequency derivative of the phase of the transfer function. For a single MRR in the over coupling regime, the resonance GD is positive to generate slow light, while for a single MRR in the under coupling regime, it is negative to produce fast light [8]. The calculated GD response of the proposed device using the above fitting parameters is shown in Fig. 5. One can see that the proposed device possesses diverse resonance GDs corresponding to different coupling regimes, rather than a monotonous resonance GD as for a single MRR. Larger magnitude of resonance GD can be achieved at the cost of lower transmission intensity when approaching the critical coupling condition.

We perform the fast/slow light experiment using the fabricated device to verify the phase responses of multiple coupling regimes. The experimental setup is shown in Fig. 6. A return-to-zero (RZ) pulse train with a duty cycle of 50% is generated by two cascaded Mach Zehnder modulators (MZMs). The first MZM is driven by a 5-Gb/s pseudo-random bit sequence (PRBS) signal with a pattern length of $2^7 - 1$, and the second one is used as a pulse carver driven by a radio frequency (RF) signal with the same rate. An erbium-doped fiber amplifier (EDFA) is used to amplify the generated probe signal followed by a tunable band-pass filter (BPF) to suppress the amplified spontaneous emission (ASE) noise. A polarization controller (PC) is inserted before the device under test (DUT) to make sure that the input probe signal is TE polarized. The output pulse train is amplified by two-stage EDFAs and two more BPFs are utilized to suppress the ASE noise. For intuitive

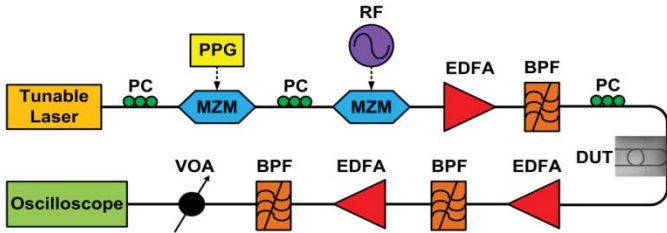


Fig. 6. Experimental setup for the observation of fast and slow lights.

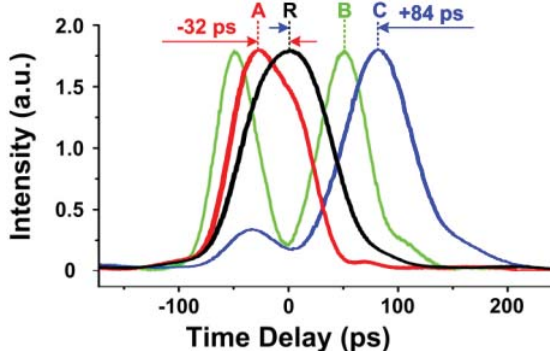


Fig. 7. Experimentally measured temporal waveforms R (black), A (red), B (green), and C (blue) of 5-Gb/s RZ pulse when the wavelength of the CW light is at points R, A, B, and C in Fig. 4(b), respectively.

comparisons, a variable optical attenuator (VOA) is employed to adjust the peak power of the advanced/delayed pulses so that it could be approximately equal to the initial one. Their temporal waveforms are recorded with an oscilloscope.

We tune the wavelength of the continuous-wave (CW) light generated by the tunable laser in Fig. 6 to measure the pulse advancement/delay. As labeled in Fig. 4(b), points A, B, and C correspond to three resonance wavelengths at different resonance notches, and point R corresponds to the reference wavelength out of the notches. Firstly, we set the signal wavelength off-resonance at point R and take the corresponding pulse waveform as a reference, shown by curve R in Fig. 7. Then we tune the wavelength to the resonance notch at point A and observe that the pulse is advanced by ~ 32 ps, as shown by curve A in Fig. 7. When the wavelength is tuned to another resonance notch at point C, a pulse delay of ~ 84 ps is observed as shown by curve C in Fig. 7. The experimentally observed pulse advancement/delay is a net result of various frequency components in the pulse bandwidth, thus it is smaller than the resonance GD in Fig. 5. Particularly, when we tune the wavelength to the deepest notch at point B, a waveform similar to that in [18] with pulse-splitting is observed as shown by curve B in Fig. 7, which indicates the approaching of the critical coupling condition. The observed fast and slow lights for resonance notches $1' \sim 9'$ in Fig. 4(b) are shown in Table II, with smaller magnitude of pulse delay when the resonance notch is farther from the deepest one at point B.

V. CONCLUSION

In conclusion, we have proposed and demonstrated a nested configuration of silicon MRR realizing multiple coupling regimes of over coupling, under coupling and quasi-critical

coupling in one passive device. The intensity responses of multiple coupling regimes have been demonstrated by resonance notches with various depths and 3-dB bandwidths in the measured transmission intensity spectrum. The phase responses of multiple coupling regimes have also been verified by experimental observation of pulse advancement, delay and splitting at different resonance wavelengths. The proposed device provides a simple way to approach the critical coupling condition, which is difficult in conventional MRRs due to fabrication uncertainties. Without incorporation of active tuning components, the complexity and fabrication cost of such device can be reduced. Moreover, the versatility of intensity and phase responses would also be useful for signal processing at various wavelengths.

REFERENCES

- [1] S. Feng, T. Lei, H. Chen, H. Cai, X. Luo, and A. W. Poon, "Silicon photonics: From a microresonator perspective," *Laser Photon. Rev.*, vol. 6, no. 2, pp. 145–177, Apr. 2012.
- [2] L. Zhou and A. W. Poon, "Electrically reconfigurable silicon microring resonator-based filter with waveguide-coupled feedback," *Opt. Express*, vol. 15, no. 15, pp. 9194–9204, 2012.
- [3] Q. Xu, B. Schmidt, S. Pradhan, and M. Lipson, "Micrometer-scale silicon electro-optic modulator," *Nature*, vol. 435, no. 19, pp. 325–327, 2005.
- [4] M. Först, J. Niehusmann, T. Plötzing, J. Bolten, T. Wahlbrink, C. Moormann, and H. Kurz, "High-speed all-optical switching in ion-implanted silicon-on-insulator microring resonators," *Opt. Lett.*, vol. 32, no. 14, pp. 2046–2048, 2007.
- [5] F. Xia, L. Sekaric, and Y. Vlasov, "Ultracompact optical buffers on a silicon chip," *Nat. Photon.*, vol. 1, no. 1, pp. 65–71, 2007.
- [6] J. Wang, and D. Dai, "Highly sensitive Si nanowire-based optical sensor using a Mach-Zehnder interferometer coupled microring," *Opt. Lett.*, vol. 35, no. 24, pp. 4229–4231, 2010.
- [7] Q. Li, Z. Zhang, J. Wang, M. Qiu, and Y. Su, "Fast light in silicon ring resonator with resonance-splitting," *Opt. Express*, vol. 17, no. 2, pp. 933–940, 2009.
- [8] F. Liu, Q. Li, Z. Zhang, M. Qiu, and Y. Su, "Optically tunable delay line in silicon microring resonator based on thermal nonlinear effect," *IEEE J. Sel. Topics Quantum Electron.*, vol. 14, no. 3, pp. 706–712, May/Jun. 2008.
- [9] T. Ye, Y. Zhou, C. Yan, Y. Li, and Y. Su, "Chirp-free optical modulation using a silicon push-pull coupling microring," *Opt. Lett.*, vol. 34, no. 6, pp. 785–787, 2009.
- [10] D. Adams, A. Aboketaf, and S. Preble, "Robust phase-shift-keying silicon photonic modulator," *Opt. Express*, vol. 20, no. 16, pp. 17440–17447, 2012.
- [11] M. Chang, M. Lee, and M. C. Wu, "Variable bandwidth of dynamic add-drop filters based on coupling-controlled microdisk resonators," *Opt. Lett.*, vol. 31, no. 16, pp. 2444–2446, 2006.
- [12] T. Kominato, Y. Hibino, and K. Onose, "Silica-based finesse-variable ring," *IEEE Photon. Technol. Lett.*, vol. 5, no. 5, pp. 560–562, May 1993.
- [13] W. Sacher, *et al.*, "Controlled coupling in silicon microrings for high-speed, high extinction ratio, and low-chirp modulation," in *Proc. CLEO*, Baltimore, MD, May 2011, pp. 1–2, Paper PDPA8.
- [14] M. Chang, M. Lee, and M. C. Wu, "Tunable coupling regimes of silicon microdisk resonators using MEMS actuators," *Opt. Express*, vol. 14, no. 11, pp. 4703–4712, 2006.
- [15] A. Yariv, "Critical coupling and its control in optical waveguide-ring resonator systems," *IEEE Photon. Technol. Lett.*, vol. 14, no. 4, pp. 483–485, Apr. 2002.
- [16] R. Ji, *et al.*, "Microring-resonator-based four-port optical router for photonic networks-on-chip," *Opt. Express*, vol. 19, no. 20, pp. 18945–18955, 2011.
- [17] Q. Chen, Y. Yang, and Y. Huang, "Distributed mode coupling in microring channel drop filters," *Appl. Phys. Lett.*, vol. 89, no. 6, pp. 061118-1–061118-3, Aug. 2006.
- [18] F. Liu, *et al.*, "Compact optical temporal differentiator based on silicon microring resonator," *Opt. Express*, vol. 16, no. 20, pp. 15880–15886, 2008.